Computational and Experimental Verification of Far-Field Mathematical Absorber Reflection Suppression

S.F. Gregson[#1], J. McCormick[*2], B.J. Kerse[*3], A.C. Newell[#4], G.E. Hindman[#5]

[#]*Nearfield Systems Inc.*

19730 Magellan Drive, Torrance, CA 90502, USA

[1]*sgregson@nearfield.com*

[4]*anewell@nearfield.com*

[5]*ghindman@nearfield.com*

[*]*Selex Galileo*

Crewe Toll, Edinburgh, EH5 2XS, UK

[2]*john.mccormick2@selexgalileo.com*

[3]*brian.kerse@selexgalileo.com*

***Abstract*— The Mathematical Absorber Reflection Suppression (MARS) technique which is used to identify and supress effects of spurious scattering within antenna measurement systems is demonstrated and its effectiveness examined through computational electromagnetic simulation and actual range measurements which were taken using a dual cylindrical reflector compact antenna test range.**

I. Introduction

The Compact Antenna Test Range (CATR) at SELEX Edinburgh is a dual reflector test facility enclosed in a 24 m by 14 m by 9 m isolated anechoic chamber with a 4.5 m by 4.5 m by 2.5 m test zone. It is designed to make measurements of antenna performance over a bandwidth from 500 MHz to 40 GHz. Over this wide range of frequencies if absorber baffles, with their wide range of position/frequency dependant requirements, are not used a number of stray/multipath signals will inevitably be incident on the antenna under test (AUT) in the test zone. The mathematical absorber reflection suppression (MARS) processing algorithm [1, 2, 3, 4, 5, 6] has been successfully implemented on single reflector CATRs in the past [7], and this paper examines its applicability when deployed on the processing of data acquired from a dual reflector CATR.

A variety of simple horn antennas were used as the AUTs in the tests and the CATR was configured to not include any additional RAM measures to suppress multi-path and in fact, as is described in the main text, a number of large reflective structures were placed within the confines of the range to increase the levels of multi-path for the tests. Measurements between 1 GHz and 5 GHz were undertaken and the impact of using the F-MARS algorithm was assessed in terms of its applicability and limitations within such a range architecture. As well as presenting an overview of the F-MARS measurement and post processing technique which is followed by an introduction to the new computational electromagnetic (CEM) simulation tool, the paper includes a description of the measurement set up, presents indicative results and a discussion as to the implications of these results on the future deployment and development of the MARS algorithm.

II. Overview of Far-Field MARS Technique

Although it is not the main purpose of this paper to present a detailed development of the MARS measurement and post processing technique, since this has been widely reported in the open literature [1, 2, 3, 4, 5, 6, 7, 8], it is useful to summarise the principal steps as this should aid in understanding the measurements and simulations discussed within this paper. MARS is a frequency domain technique that is entirely generic in nature that requires no additional hardware, and which can be applied to a wide variety of different antenna types with no specific a priori assumptions being made about the distribution of the currents over the AUT. The F-MARS process can be summarised as follows:

1. Take a direct single frequency acquisition of the one-dimensional far electric field amplitude and phase pattern functions with the AUT offset from the origin of the measurement origin.
2. Apply a differential phase change to mathematically translate the AUT back to the origin of the measurement co-ordinate system.
3. Obtain the translated mode coefficients of the AUT.
4. Apply band pass mode filtering function to suppress unwanted higher order CMCs where the properties of the filter function are determined from the physical size of the AUT.
5. Compute far electric field pattern from filtered mode coefficients to obtain the F-MARS processed AUT pattern function.

In practice, the processing is implemented efficiently through the use of the fast Fourier transform (FFT) [8, 9]. The following section describes how this type of far-field measurement can be simulated using purely CEM techniques.

III. Introduction to CEM Range Simulation

An antenna measurement can be simulated by evaluating the complex coupling coefficient between an AUT and a near-field probe (or remote source antenna for the case of a far-

field measurement). Clearly, this must be evaluated for each point within the simulated acquisition surface, and for each sampled polarisation and frequency. In principle, it would be possible to obtain the mutual coupling coefficient between a given single mode in the waveguide port in the AUT and a single mode in the waveguide port of the scanning probe from a three-dimensional CEM full wave solver. This approach would have the advantage of introducing the least number of assumptions and approximations. Unfortunately, at the present time, although many solvers are available, these are generally considered inappropriate for simulating problem spaces as electrically large that needed to enclose a complete near- or far-field measurement system, especially when that model is to include positioners, reflectors, absorber, cranes, lights, *etc.* and is a consequence of the extended processing times and the large amounts of computer resources required. Thus, alternative, more specialised, strategies are required.

One possible technique for accomplishing this would be to utilise physical optics, and specifically the Kirchhoff-Huygens Principle which enables fields specified over one closed surface to be propagated to another point in a source or sink free region outside that closed surface [9]. This method is applicable to arbitrary closed surfaces over which both the electric *and* magnetic fields are known. When expressed mathematically, the electric field at a point P radiated by a closed, but arbitrary, Huygens' surface S is,

$$\underline{E}_p = \frac{1}{4\pi}\int_S \left[\begin{array}{l} -j\omega\mu(\underline{n}\times\underline{H})\psi + \\ (\underline{n}\times\underline{E})\times\nabla_0\psi + (\underline{n}\cdot\underline{E})\nabla_0\psi \end{array}\right] ds_0 \qquad (1)$$

Here, $\underline{E}$ and $\underline{H}$ denote the electric and magnetic fields respectively and are specified over the enclosing surface, ω is the angular frequency, k_0 is the free space propagation constant, $\underline{n}$ is the outward pointing unit normal and, respectively, ε and μ are the permittivity and permeability of the medium through which the fields are propagating, and ∇_0 is the differential vector operator expressed in the source co-ordinate system. The first order spherical function is denoted by ψ,

$$\psi = \frac{e^{-jk_0 r'}}{r'} \qquad (2)$$

Where r' is the displacement of the field point from the elemental source and is related to the co-ordinates of the elemental Huygens source $\underline{r}_0$ and the co-ordinates of the field point $\underline{r}$ through,

$$r' = \left|\underline{r} - \underline{r}_0\right| \qquad (3)$$

The geometry of this statement of the Kirchhoff-Huygens formula can be found illustrated in its conventional form in Figure 1. These expressions are amenable for evaluating the field at any point in space outside of S and as such can be used to create near- and far-field simulations alike. Any one of a number of commercial full wave three-dimensional full-wave CEM simulation tools can be harnessed to solve for the fields across the Huygens' surface whereupon the Kirchhoff–Huygens' method can be used to calculate the fields resulting from this radiator throughout a much larger (potentially infinite) problem space. In this way, measurement simulations of great accuracy and complexity can be produced comparatively simply and easily.

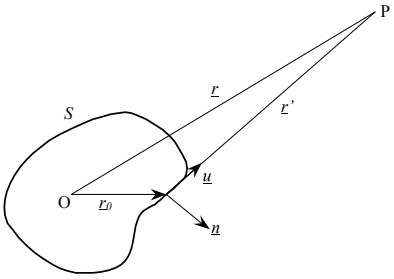

Fig. 1: Geometry of Kirchhoff-Huygens formula for the propagation of electromagnetic fields from Huygens' surface S, to point P.

Typically, when computing the far-field pattern of an antenna from knowledge of the corresponding near-fields, the vector $\underline{r}$ would be chosen so that the evaluation of the integral would produce the antenna diagram for a specified angular direction, *e.g.*,

$$\hat{\underline{r}} = \sin(Az)\cos(El)\hat{\underline{e}}_x + \sin(El)\hat{\underline{e}}_y + \cos(Az)\cos(El)\hat{\underline{e}}_z \qquad (4)$$

Here, Az and El are the azimuth and elevation angles respectively and describe a conventional azimuth over elevation spherical positioning system [9]. However, when simulating an antenna measurement facility, it is perhaps more convenient to rotate the AUT, *i.e.* the closed Huygens' surface, using a vector isometric rotation [9] and then to evaluate the far-fields in a single direction which more closely mimics the antenna measurement process and allows chamber scatterers to be introduce into the model in a direct way. In principle, either approach can be used although the latter case is perhaps more straightforward to conceptualise. In this case, $\underline{r}$ would be held fixed for all measurement angles such that,

$$\hat{\underline{r}} = 1\hat{\underline{e}}_z \qquad (5)$$

Where a z-axis directed range boresight has been chosen. Thus, the AUT can be positioned within the range as though it were installed on a conventional azimuth over elevation positioning system or, for that matter, any other arrangement of translation and or rotation stages. Thus, this technique is capable of simulating planar, cylindrical and spherical near-field test system, and spherical far-field or quasi far-field test systems. In this paper, far-field spherical test systems will be simulated such that the effectiveness of the far-field MARS measurement and post processing technique can be better determined.

A central constituent of the MARS measurement process is to offset the AUT from the centre of rotation, this can be easily incorporated within the simulation by applying an offset to the Cartesian components of the position vector that determines the location of the radiating Huygens surface where this translation is applied prior to the usual rotations. Once evaluated using the Kirchhoff-Huygens method, the resulting far-fields can be resolved from the range co-ordinate system back onto the antenna co-ordinate system by applying the inverse rotation to the far electric (and magnetic) fields where the results have been found to be in agreement with those produced using conventional processing [10]. Crucially, when introducing a given scatterer into the range simulation, the position and orientation of the scatterer is by definition

specified in the range co-ordinate system and will therefore be fixed irrespective of the particular far-field antenna pattern angle being computed. Thus, working in terms of the range co-ordinate system, as outlined above, significantly simplifies the computational processing.

The inclusion of an arbitrarily located and shaped perfectly conducting (*i.e.* worst case) scattering object can be introduced by using the Kirchhoff-Huygens field propagation method described above together with the generalised law of reflection [11]. By definition, an elemental Huygens source is considered to be infinitesimally small and so it will radiate a spherical wave. However, as the observation point on the reflecting plate is finitely far removed from the source, *i.e.* more than a few wavelengths away, the reflecting plate will be in the far-field of the elemental Huygens source. Locally at the observation point, the field will be of the form of a transverse electric and magnetic (TEM) plane wave propagating in the direction $\underline{r}$'. As the field is a local plane wave and assuming that the reflecting surface is also locally planar and is made from a perfectly conducting (PEC) material, the normal electric field component will be unchanged upon reflection. Thus, if a homogeneous plane wave is incident on a flat PEC surface of infinite extent the reflected elemental electric field constitutes a similar plane wave and the reflected field can be obtained from the incident field using [11],

$$\underline{E}_r = 2(\hat{\underline{n}} \cdot \underline{E}_i)\hat{\underline{n}} - \underline{E}_i \tag{6}$$

Thus, it is possible to write the general statement of reflection as [11],

$$\hat{\underline{u}}_r = \hat{\underline{u}}_i - 2(\hat{\underline{n}} \cdot \hat{\underline{u}}_i)\hat{\underline{n}} \tag{7}$$

Here, $\hat{\underline{u}}_i$ denotes the direction of propagation of the incident plane wave and $\hat{\underline{u}}_r$ represents the direction of propagation of the reflected, specular, plane wave. This can be taken to represent the general form of the law of reflection with the scattered field being a plane wave as the material is assumed to be infinite in extent in the tangential direction and the material properties do not vary across this infinitesimal surface. As the reflected elemental electric field correspond to a plane wave propagating in the direction $\hat{\underline{u}}_r$ the elemental magnetic field can be obtained from the elemental electric field using the TEM, *i.e.* plane wave, condition. The total reflected electric and magnetic fields at each point on the surface of the reflector can be obtained by summing all of the contributions from the infinitely many elemental Huygens sources radiating from *S*. The far scattered field can again be obtained from using the Kirchhoff-Huygens method by integrating over the surface of the reflector and thereby evaluating the far scattered fields. Ignoring blockage, the total measured far-field for a particular pattern angle can be obtained by taking the linear superposition of the direct and scattered fields. As a far-field measurement is being simulated, probe pattern effects are unimportant in this analysis and can be omitted thereby simplifying the processing (probe effects can be included as discussed in [9]). Thus, by following this process, a simulation of a typical MARS type far-field measurement can be created with almost complete freedom. Details of the application of this CEM model are detailed in the following section.

IV. Results of CEM F-MARS Range Simulation

In order that the F-MARS measurement and post-processing technique could be further verified, a far-field measurement was simulated that recreated a typical F-MARS measurement configuration, *c.f.* [7, 8]. A commercially available three-dimensional full wave CEM solver was used to simulate the near-fields radiated by a WR90 open-ended rectangular waveguide (OEWG) section that was excited by the fundamental TE_{10} mode. The Cartesian components of the electric and magnetic fields were obtained at 10 GHz specified across the surface of an ellipsoid that tightly bounded the radiating aperture. The maximum radial extent of this ellipsoid when displaced from the origin was 0.08 m. The aperture of the OEWG section was displaced from the origin of the range measurement co-ordinate system, *i.e.* the centre of rotation, by 0.1 m in the AUT z-axis which was specified as being at a normal to the waveguide aperture plane. This had the effect of centring the ellipsoid about the aperture of the OEWG. A square PEC reflecting plate of side 0.3 m was introduced into the simulation located with its centre at x =-0.1 m, y = 0 m, z = 1.0 m. This configuration closely mimicked a number of configurations that had previously been used to verify the F-MARS technique experimentally. The physical-optics based simulation was then used to obtain the far-electric field great circle azimuth cut with a range length of 200 m which placed the AUT in the far-field.

The results of this simulation can be found presented below in Figure 2 which contains the far-field great circle cardinal cut of the amplitude antenna pattern which is denoted by the blue trace (*i.e.* the far-field pattern of antenna in the presence of the reflecting flat plate). This is plotted together with the equivalent pattern cut for the antenna in the absence of the reflecting plate, red trace. This clearly reveals the impact of the scatterer on the far-field pattern. The magenta trace comprises the equivalent multi-path level (EMPL) [9] which can be thought of as comprising a measure of the degree of similarity (*i.e.* adjacency) between two patterns. As has been see previously with actual range measurements, the reflecting plate induces a perturbation to the antenna pattern at specific angular regions where the error to signal level is as little as *circa* 15 dB (-30 dB EMPL). This is also clearly visible in this simulation where the plate is illuminated twice within a single 360° cut with the two specular directions being separated by 180° which results from the poor front to back ratio of the OEWG which is *circa* 10 dB. This ripple is a result of the direct and indirect (*i.e.* scattered) signals adding constructively and destructively as the AUT is rotated. A detailed description of the validation of this CEM model can be found presented in the open literature [10] where it was used to verify the empirically derived rules used for acquiring data for F-MARS processing. During that investigation, it was noted that the choice of band pass filter function could subtly influence the F-MARS processed far-field pattern data. As a consequence of this, the behaviour of various band pass windowing functions [12] was investigated further. To this

end, Figure 3 contains a plot of the far-field great circle azimuth cut of the OEWG which is denoted as the red trace, this represents the ideal "truth" model against which the F-MARS processed patterns can be compared.

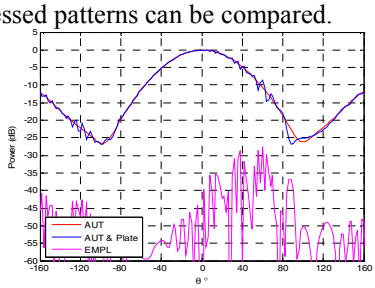

Fig. 2 Plot of the far-field pattern of the AUT with and without the reflecting plate. The specular reflection from the AUT evident in pattern & EMPL plots.

The equivalent pattern with the reflecting plate can be seen plotted in blue. The black trace represents the F-MARS processed pattern with the magenta trace showing the EMPL which was formed by comparing the ideal AUT pattern and the F-MARS processed pattern. Here, it can be seen that in the specular direction the error to signal level has increased significantly to in excess of 40 dB. The peak EMPL has also improved by circa 20 dB from -27 dB to -47 dB thereby verifying the effectiveness of the F-MARS technique. Figure 4 presents the equivalent cylindrical mode coefficient (CMC) plots with (blue trace) and without (red trace) F-MARS filtering. Here, it is clear that, in common with previous implementations of F-MARS, a rectangular (Dirichlet) [12] band pass window was applied to the spectrum of CMCs. Close inspection of the F-MARS processed pattern shown in Figure 3 reveals that there is some degree of spurious ringing evident on the far-field pattern. This was thought to be a result of spectral leakage [12] which was exacerbated by the comparatively large discontinuity encountered at the spectrum band edges. As a consequence of this, the F-MARS processing was repeated employing a number of alternative, commonly used, candidate windowing functions that better matched the function and its derivatives to zero at the edges of the band than was the case for the baseline rectangular filter function. These windowing functions included: Triangular (Bartlet), $\cos^{\alpha}$, Gaussian, windowing functions *etc.*. Of these, the Gaussian and $\cos^2$ windows were found to yield the most encouraging results. Figure 5 and 6 below contain equivalent plots to Figure 3 and 4 respectively for the case where a $\cos^2$ window had been applied. From inspection it is clear that the EMPL has reduced by more than 5 dB in the specular direction and the high angular frequency angular ripple (*i.e.* ringing) that was evident previously on the Dirichlet filtered F-MARS pattern has been very successfully suppressed.

Typically, the use of windowing functions is avoided when taking antenna measurements as in certain circumstances they can fail to maintain the integrity of the underlying antenna pattern function. In this area of application however, the higher order CMCs are excluded on physical grounds as they are unable to contribute to the far-field radiating antenna pattern function. The spectral leakage that has been observed in some simulations is an artefact of the discontinuity in the discrete spectrum of CMCs once the band pass filter function has been applied and better satisfying the Dirichlet boundary conditions which is mandatory for successful use of the discrete Fourier transform and is therefore justifiable. As trigonometric functions are well behaved and readily computed this window was utilised when processing the range measurements described in the following section.

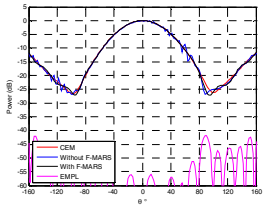

Fig. 3 Far-field pattern of AUT showing ringing from Dirichlet filter

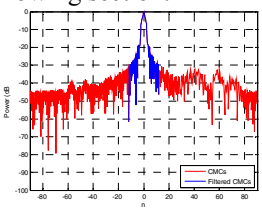

Fig. 4 Equivalent CMCs with Dirichlet window applied.

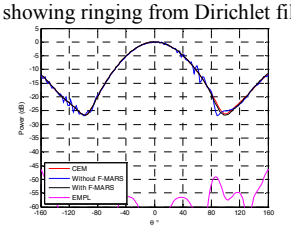

Fig. 5 Far-field pattern of AUT with ringing effectively suppressed.

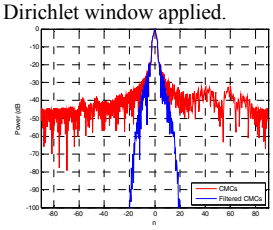

Fig. 6 Equivalent CMCs with $\cos^2$ window applied.

V. The CATR Measurements

A number of standard gain horns (SGH) were used as the AUTs and they were sequentially displaced from the centre of rotation of the range using one of the translational axes in the antenna positioner within the range, to positions 300 mm to 600 mm off centre. Also to provide additional scattering in a number of the measurements, using a low RCS column, a large rectangular metal plate 80 cm by 80 cm was placed some 3 metres from the antenna at 130° off boresight to the AUT and a number of the measurements were repeated. Measurements were undertaken at 1 GHz and 5 GHz with the antenna displaced off centre by varying amounts. The measurements showed that the F-MARS processing was effective and that the multipath in evidence in the measurements as a result of the presence of scattering in the chamber could be removed at many, and suppressed at all angles.

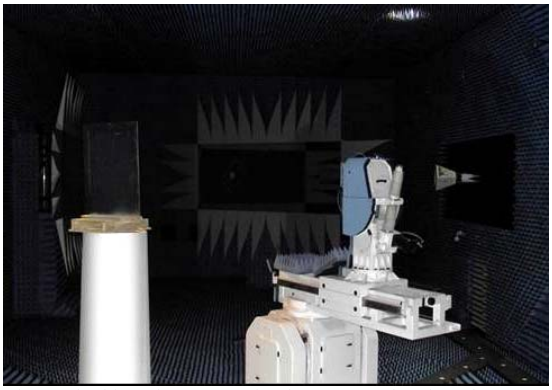

Fig. 7 Picture looking downrange in the CATR showing the AUT on the positioner and the flat rectangular scatterer placed on a low RCS polystyrene column to increase the scattering in the chamber (shown to left).

Figures 8 and 9 are illustrative examples of the action of the F-MARS processing in the range and how it reduces the

effects of scattering. Figures 10 and 11 show the action of the F-MARS processing when a large scatterer in this case a large metal plate, as shown in figure 7, was placed in the proximity of the AUT and the antenna was not offset from the centre of rotation. Finally figure 12 and 13 clearly shows the improvement that can be obtained using the F-MARS processing when an offset in the AUT position is used even in the presence of such a large scattering object.

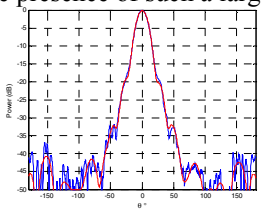

Fig.8 Amplitude with, (red) and without, (blue) F-MARS: taken without plate located at origin.

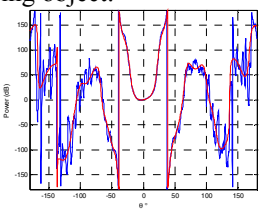

Fig.9 Phase with, (red) and without, (blue) F-MARS: taken without plate located at origin.

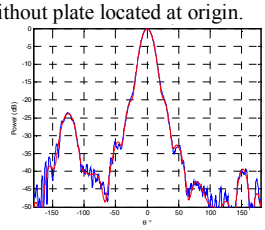

Fig.10 Amplitude with, (red) and without, (blue) F-MARS: taken with plate located at origin.

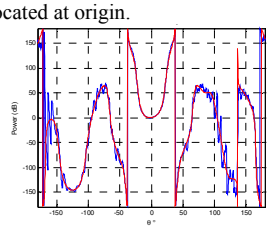

Fig.11 Phase with, (red) and without, (blue) F-MARS: taken with plate located at origin.

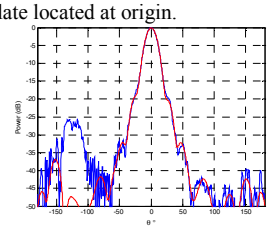

Fig. 12 Amplitude. With, (red) and without, (blue) F-MARS: taken with plate offset from origin.

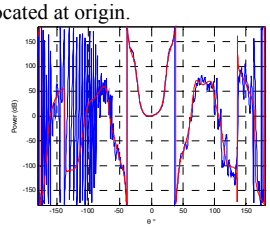

Fig. 7 Phase with, (red) and without, (Blue) F-MARS: taken with plate offset from origin.

Clearly these figures show the extent to which the fidelity of measurements that are severely degraded by scattering may be improved by the use of the F-MARS processing with the only penalty being the increase in the amount of data acquired as a result of the increase in the minimum sphere [9] that the AUT occupies as a result of the offset in its position during the course of the measurements.

VI. Summary and Conclusions

Far-field MARS processing can be used with a very high degree of confidence since all the steps in the measurement and analysis are consistent with the well-established principles of standard cylindrical near-field theory and measurement technique, and all comparisons thus far have proved overwhelmingly positive. The offset of the AUT and the resulting finer sample spacing are estimated using conventional rules, and the mathematical translation of the AUT to the origin is rigorous. The selection of the mode cut-off for the translated pattern is based on the physical dimensions of the AUT and its translated location. The final result with F-MARS processing can be degraded if the translation of the AUT is incorrectly applied, or the mode filter is too tight, but these parameters are controlled by the user. Clearly, the results of far-field MARS processing will reduce but cannot entirely eliminate the effect of scattering. As has been demonstrated, this novel frequency domain measurement and processing technique is entirely general, even when testing lower gain antennas. MARS has been found to improve the reflection levels in traditional anechoic chambers allowing improved accuracy as well as offering the ability to use existing chambers down to lower frequencies than the absorber might otherwise suggest.

However the suppression of the multipath signal is not complete at all angles. As can be seen in figure 12, although the effects of the multi-path have been largely removed they are still present as can be seen from the asymmetry in the pattern beyond -150^0 degrees – which is in the back half space. The effects that the comparatively small electrical distance of the scatterer from the AUT have yet to be examined in detail and the extent to which the processing is effective with respect to cross range position of the antenna at different angles is also a variable that needs to be investigated. However, overall effectiveness of the techniques, as implied by the modelling, was clearly demonstrated in the measurements undertaken within the dual reflector CATR.

References

[1] G.E. Hindman, A.C. Newell, “Reflection Suppression in a large spherical near-field range”, AMTA 27th Annual Meeting & Symposium, Newport, RI, October. 2005.

[2] G.E. Hindman, A.C. Newell, “Reflection Suppression To Improve Anechoic Chamber Performance”, AMTA Europe 2006, Munich, Germany, March 2006.

[3] S.F. Gregson, A.C. Newell, G.E. Hindman, “Reflection Suppression In Cylindrical Near-Field Antenna Measurement Systems – Cylindrical MARS”, AMTA 31st Annual Meeting & Symposium, Salt Lake City, UT, November 2009.

[4] S.F. Gregson, A.C. Newell, G.E. Hindman, M.J. Carey, “Advances in Cylindrical Mathematical Absorber Reflection Suppression”, 4th European Conference on Antennas and Propagation, Barcelona, 12th - 16th April, 2010.

[5] S.F. Gregson, A.C. Newell, G.E. Hindman, M.J. Carey, "Extension of The Mathematical Absorber Reflection Suppression Technique To The Planar Near-Field Geometry", AMTA, Atlanta, October 2010

[6] S.F. Gregson, A.C. Newell, G.E. Hindman, M.J. Carey, “Application of Mathematical Absorber Reflection Suppression to Planar Near-field Antenna Measurements”, 5th European Conference on Antennas and Propagation, Rome, 11th – 15th April, 2011.

[7] S.F. Gregson, J. Dupuy, C.G. Parini, A.C. Newell, G.E. Hindman, "Application of Mathematical Absorber Reflection Suppression to Far-Field Antenna Testing", LAPC 2011, Loughborough, November 2011.

[8] S.F. Gregson, B.M. Williams, G.F. Masters, A.C. Newell, G.E. Hindman, "Application of Mathematical Absorber Reflection Suppression To Direct Far-Field Antenna Range Measurements", AMTA, Denver, October 2011.

[9] S.F. Gregson, J. McCormick, C.G. Parini, “Principles of Planar Near-Field Antenna Measurements”, The Institution of Engineering and Technology, UK, 2007.

[10] S.F. Gregson, A.C. Newell, G.E. Hindman, "Examination of Far-Field Mathematical Absorber Reflection Suppression Through Computational Electromagnetic Simulation", International Journal of Antennas and Propagation, Special Issue on Recent Advances in Near-Field to Far-Field Transformation Techniques, March 2012.

[11] R.H. Clarke, J. Brown, “Diffraction Theory and Antennas”, Ellis Horwood Ltd., 1980.

[12] F.J. Harris, “On the Use of Windows for Harmonic Analysis with the Discrete Fourier Transform”, Proc. IEEE Vol. 66, No. 1, pp. 51 – 83, January 1978.